UC Riverside
BCOE Research

Title

ECEF Position Accuracy and Reliabilityin the Presence of Differential Correction Latency Year 1 Technical Report for Sirius XM

Permalink

https://escholarship.org/uc/item/38d3h08w

Authors

Rahman, Farzana
Aghapour, Elahe
Farrell, Jay

Publication Date

2018-10-29

eScholarship.org Powered by the California Digital Library
University of California

ECEF Position Accuracy and Reliability in the Presence of Differential Correction Latency

Year 1 Technical Report for Sirius XM

Farzana Rahman, Elahe Aghapour and Jay A. Farrell
Department of Electrical and Computer Engineering,
University of California, Riverside, 92521.
{frimi, eaghapour, farrell}@ece.ucr.edu

Executive Summary

Commercial on-vehicle implementation of Earth-referenced positioning at submeter accuracy with 99% probability would require widely and reliably available differential corrections; however, such corrections delivered on a nationwide or global scale via satellite systems will incur latency between their time-of-applicability and their time-of-reception at the vehicle.

This report summarizes the conclusions of the first phase of work performed by University of California, Riverside (UCR). There were two main goals for this one-year effort.

1) To investigate the sensitivity of differential Global Navigation Satellite System (DGNSS) corrections and position estimation accuracy to communication latency.
2) To investigate the feasibility of achieving meter-level positioning accuracy at least 95% of epochs.

The first phase of this project was designed to study stationary receivers, to clearly define, demonstrate, and address the challenging issues. In this study, all algorithms use identical data sets (i.e., measurements and corrections); therefore, the study compares the performance of different algorithms using the same data.

Two conference articles resulted from the first phase of the project [1], [2]. Article [1] considers both latency effects and positioning accuracy using Kalman filtering methods. Article [2] considers position estimation accuracy in the presence of outliers both by Kalman filtering and by risk-averse performance-specified state estimation (See Appendix C). This report combines the results of both papers.

The first conclusion is that GNSS corrections can be designed such that position estimation accuracy is robust to correction latency up to 600 seconds. This is demonstrated via experiments that are described in Section VI. The method of GNSS correction calculation is described in Section IV with results of example computations in Appendix A.

The second conclusion is that meter-level horizontal position accuracy is achievable in excess of 99% of the samples when a sufficient number of satellites are observable with appropriate geometry, both pseudorange and Doppler measurements are used, and outlier measurements are suitably accommodated. Since DGNSS is designed to remove the effects of common mode errors, this study pays special attention to accommodation of the non-common mode errors. A main issue is accommodating multipath. The importance of the Doppler measurement for addressing multipath is motivated in Section V-B and demonstrated in Fig. 4. Experimental demonstration results are included in Sections VI and VII.

Many applications, including connected and autonomous vehicles, would benefit from navigation technologies reliably achieving sub-meter position accuracy with high reliability for a moving receiver. The second phase of this project will study the feasibility of achieving the position accuracy specification for a moving receiver combined with a commercial grade inertial measurement unit. The results herein used a local base station approach. National or global implementations would be more efficient using networks of base stations working collaboratively to estimate parameters usable by user receivers to reconstruct corrections. Such methods are the focus of phase three of the study.

This study focuses on single frequency, single constellation results. The availablility of multiple constellations and multiple frequencies per constellations will facilitate compensation of ionospheric error, accommodation of outliers, and accommodation of multipath while still having a set of satellites with appropriate geometry to reliably achieve the performance specification.

CONTENTS

I Introduction 3

II Related Work 3

III GNSS Background 3
- III-A Notation . . . 3
- III-B Models . . . 4
- III-C Measurement Errors . . . 4

IV DGNSS Correction Approach 4
- IV-A Local DGNSS Corrections . . . 4
- IV-B Filtering to Decrease Non-common Mode Errors Effects . . . 5

V Position Estimation 5
- V-A System Model . . . 5
- V-B Simplified Illustrative Example . . . 6

VI Experimental Results: Latency Effects 7
- VI-A Experimental Data Description . . . 7
- VI-B Correction Sensitivity to Latency . . . 7
- VI-C Position Estimation Algorithms . . . 7
- VI-D Positioning Accuracy . . . 7
- VI-E Positioning Sensitivity to Latency . . . 8

VII Experimental Results: Position Accuracy with Outliers 8
- VII-A Outlier Generation . . . 8
- VII-B State Space Model . . . 8
- VII-C State Estimation Algorithms . . . 9
- VII-D Performance Metrics . . . 9
- VII-E Experimental Results: Single Run . . . 9
- VII-F Experimental Results: Monte Carlo . . . 10

VIII Conclusion and Future Work 10

IX Acknowledgement 10

References 10

Appendix 12
- A Example Computed Corrections . . . 12
- B Kalman Filter Design . . . 13
- C Risk-Averse Performance-Specified State Estimation . . . 14

Copyright ©2018, University of California, Riverside. All Rights reserved.

I. Introduction

A new generation of applications (e.g., autonomous vehicles, connected vehicles, and driver's assistance applications [3], [4]) are placing much stricter accuracy and reliability specifications on navigation systems than was required for the previous generation of personal navigation devices. Over the last several decades, Global Navigation Satellite Systems (GNSS) have become dominant for personal and vehicular navigation. Standard GNSS accuracy of about 10 m [5], [6] has typically been sufficient.

The FHWA, state DOTs, and auto manufacturers are investigating connected and autonomous highway vehicle applications which will benefit from real-time, ECEF position estimates accurate to sub-meter level at 99% probability. Pilot projects are ongoing in at least three locations [7]–[9]. The objectives include improving roadway network safety and throughput, while decreasing emissions impact.

Commonly cited position accuracy levels derived from differential GNSS (DGNSS) are 1-3 meters [10]. The lower end of this range approaches the sub-meter specification, if this accuracy can be achieved with sufficient reliability and if it is not sensitive to DGNSS correction communication latencies.

Navigation systems achieving these accuracy and reliability specifications have not yet been demonstrated. For a national scale of implementation, topics of interest include: communication physical layers, network design for real-time applications, position error sensitivity to communication latency, and estimation algorithms to achieve the accuracy specification.

This technical report studies position estimation accuracy as a function of communication latency. It discusses modeling and estimation algorithm choices as they affect positioning algorithm performance. Section III presents notation and background related to the measurement and models. Section IV presents the differential correction latency compensation approach that is used herein. Section V discusses the state-space model used by the state estimation algorithms. It also includes a simplified example designed to motivate the use of the Doppler measurement to improve the ability to discriminate and accommodate multipath errors. The approach augments one multipath state per satellite. The results show that using the Doppler measurement significantly enhances the degree-of-observability. Section VI presents experimental results that demonstrate meter-level positioning performance that is robust to correction latency. Section VII presents experimental results studying the effect of outliers on different state estimation algorithms.

The results discussed herein were first reported in [1], [2].

II. Related Work

Vehicle positioning by DGNSS is a well researched area [11]–[17]. The literature presents extensive position estimation theory, algorithm, and experimental results that illustrate alternative modeling choices and their impact on performance and reliability [18]–[21].

One important aspect of DGNSS positioning is the sensitivity of position error to baseline separation and communication latency. References [22]–[25] present methods to construct networked differential correction services, ultimately leading to nationwide differential correction service (e.g., WAAS, EGNOS). Various pre-2001 papers [14], [15], [26]–[29] characterize the degradation of positioning accuracy as a function of latency in the era of selective availability (SA). Due to the design of SA, the correction error and hence the position error grew rapidly over tens of seconds. Methods to compensate for communication latency over low bandwidth channels for real-time applications are discussed in [14], [15]. Until recently [1], the literature lacked studies of real-time positioning performance versus correction latency in the post-SA data.

Multipath error is the dominant error source in differentially corrected GNSS measurements. The literature provides a few methods to address the issue. In [30], the author introduces a narrow correlator based tracking loop system that provided a 20 to 50 percent reduction in multipath error effects for the L1 pseudorange measurement. In [31], [32], multipath error modeling is addressed using dual frequency carrier phase measurements in a GNSS antenna array system. Choke ring antennae [33] are another option, but are not practical for inexpensive on-vehicle applications. Lastly, many implementations augment one (or more) multipath states per satellite to the state vector. Use of Doppler measurement improves positioning performance by estimating the velocity [34]–[37]. A less well understood benefit of the Doppler measurement is that it enhances the degree-of-observability of the multipath states. This topic will be discussed in Section V.

III. GNSS Background

This section introduces notation and the GNSS measurement models. For additional information on GNSS, see [18], [19], [21].

GNSS receivers provide three different types of measurements: pseudorange, Doppler and carrier phase. At present, these signals are available to civilians only on the L1 frequency. This study focuses pseudorange and Doppler L1 measurements for the GPS constellation.

In the near-term, low-cost consumer receivers are expected to provide additional measurements from multiple constellations and at multiple frequencies for GPS (i.e., L1, L2, and L5). The methods that we discuss will generalize to such situations with only minimal algorithmic changes. These additional measurements will enhance performance further and facilitate implementations. For example, measurements at multiple frequencies will improve real-time estimation of ionospheric delays with or without a base station.

A. Notation

To clearly distinguish between models and computations this report will use two different symbols. The symbol $\doteq$ indicates that the equation is a model. Models are used to analyze, understand, and physically interpret measurements, often with the goal of designing algorithms to estimate quantities that are of interest (e.g., position). The symbol $=$ indicates that an equation represents an actual algorithmic calculation.

Copyright ©2018, University of California, Riverside. All Rights reserved.

When it is necessary to represent both the actual and computed versions of a variable, x will represent the actual value while $\hat{x}$ will represent the computed value. For example, p^s represents the actual position of satellite s while $\hat{p}^s$ represents the position of satellite s computed from the available ephemeris data.

B. Models

The pseudorange measurement model is

$$\rho_r^s \doteq R(p_r, p^s) + ct_r - ct^s + I^s + T^s + M_r^s + \eta_r^s \tag{1}$$

where the range between a receiver location p_r and a satellite location p^s is

$$R(p_r, p^s) = |p_r - p^s|. \tag{2}$$

The symbol ct_r represents the receiver clock bias, ct^s is the residual satellite clock bias after ephemeris corrections, I^s is ionospheric error, T^s is tropospheric error, M_r^s is multipath error, and η_r^s is random noise affecting the pseudorange measurement.

The Doppler D_r^s measurement model is

$$\lambda D_r^s \doteq (h^s)^T (v_r - v^s) + cb_r - cb^s + \varepsilon_r^s \tag{3}$$

where the line-of-sight vector from satellite s to receiver r is

$$h^s = \frac{p_r - p^s}{|p_r - p^s|}. \tag{4}$$

The symbols v_r and v^s represent the receiver and satellite velocity vectors, cb_r and cb^s are the receiver and satellite clock drift rates, and ε_r^s is random measurement noise affecting the Doppler measurement.

C. Measurement Errors

The pseudorange measurement has 7 types of errors, (see Sections 1.2-1.3 of [10] and [38]). They can be classified into two categories:

- *Common-mode errors* (ephemeris, satellite clock bias, ionosphere, troposphere) are common to all receivers in the same vicinity and can be mitigated with the use of DGNSS corrections.
- *Noncommon-mode errors* (receiver clock bias, multipath, receiver noise) are different for each receiver.

This report discusses methods to manage both types of errors to achieve sub-meter positioning accuracy.

IV. DGNSS Correction Approach

This section discusses DGNSS technique and delineates various issues that must be addressed toward achieving sub-meter positioning accuracy. DGNSS is the typical approach to remove common-mode errors from pseudorange measurements [10], [13], [18].

All DGNSS approaches use at least one base station with a high quality receiver and antenna located at a mechanically stable and known location p_b. Due to the antenna location being stationary and known, the DGNSS approach can estimate corrections for roving receivers, enabling significant enhancement in rover position estimation accuracy, assuming that the corrections can be communicated to the rovers.

DGNSS can be implemented on local, regional or global scales. Local DGNSS approaches are the easiest to understand. The standard basic approach is described in detail in Section IV-A. Regional and global approaches utilize a network of GNSS receivers. The measurements from the network are combined to estimate correction information that is broadcast to users, such that each user can reconstruct a local correction [23], [24]. For commercial DGNSS applications on a global scale, network DGNSS methods are likely to be the most feasible for a few reasons. First, the number of base stations is significantly reduced relative to local approaches implemented worldwide. Second, a single entity responsible for the network of base stations can implement measures to ensure and verify integrity. Third, commercial entities utilizing the corrections (e.g., car manufacturers) could interact with a single standard (e.g., data format and communication physical layer) globally rather than numerous local standards.

The collection of data from remote base receivers, computation and verification of corrections, and communication of corrections to users results in *latency* ℓ between the time-of-applicability t_0 and the time that it is actually used $t_0 + \ell$. Robustness to communication latency is critical.

A primary goal of this study is to evaluate the sensitivity of positioning accuracy to communication latency. For the purpose of this study, it is sufficient to utilize local corrections. The local approach used in this paper, described in Section IV-B, is a variant of the RTCM standard [11].

For the approach herein, the correction convergence time at the rover is zero seconds, once the base station message is received. For alternative approaches, such as those based on precise point positioning [10], [39], [40], the convergence time is non-zero, so the results of this study would not be applicable.

A. Local DGNSS Corrections

This section discusses a local base station algorithm that is essentially compatible with the RCTM standard. The local base station position P_b is known.

At time t the base station algorithm computes

$$\tilde{c}^s(t) = \rho_b^s(t) - R(p_b, \hat{p}^s(t)) - c\hat{t}_b(t) + c\hat{t}^s(t) \tag{5}$$

where ρ_b^s is the base pseudorange measurement, $R(p_b, \hat{p}^s) = |p_b - \hat{p}^s|$, $\hat{p}^s$ and $\hat{t}^s$ are the satellite position and clock bias computed from ephemeris data, and $c\hat{t}_b(t)$ is an estimate of the base receiver clock bias.

The model for $\tilde{c}(t)$ is

$$\tilde{c}^s(t) \doteq I^s(t) + T^s(t) + E^s(t) - c\delta t^s(t) + M_b^s(t) + \eta_b^s(t) \tag{6}$$

where $E^s = R(p_b, p^s) - R(p_b, \hat{p}^s)$ is satellite ephemeris error and $c\delta t^s = ct^s - c\hat{t}^s$ is residual satellite clock bias. Note that all of the terms on the right-hand side of eqn. (6) are unknown. The goal is that the broadcast correction to the rover should allow accurate prediction of the common-mode error

$$I^s(t) + T^s(t) + E^s(t) - c\delta t^s(t),$$

Copyright ©2018, University of California, Riverside. All Rights reserved.

while being minimally influenced by the base station noncommon-mode error

$$M_b^s(t) + \eta_b^s(t).$$

Eqn. (6) shows that $\tilde{c}^s(t)$ contains both common and noncommon-mode errors; therefore, additional processing is desirable.

B. Filtering to Decrease Non-common Mode Errors Effects

Each noncommon-mode error source is correlated over only a few minutes whereas the common-mode error sources are correlated over several hours. Due to this frequency separation, various forms of low-pass filtering should attenuate the affects of the noncommon-mode errors.

Before filtering, it is useful to consider the ionospheric delay. When the ionospheric delay rate is high, a low-pass filtered correction would lag the present value of $\tilde{c}^s(t)$. The ionospheric delay has trends that are largely predictable using satellite data available at each base and rover. Therefore, the predictable portion of these terms is removed prior to filtering and added back into the filtered results.

Let $\hat{I}^s$ represents the ionosphere delay computed using satellite data. Using this predicted ionospheric delay produces the new computed variable

$$\tilde{d}^s(t) = \tilde{c}^s(t) - \hat{I}^s(t). \tag{7}$$

The model for $\tilde{d}^s(t)$ is

$$\begin{aligned} \tilde{d}^s(t) \quad &\doteq \quad \delta I^s(t) + T^s(t) + E^s(t) - c\delta t^s(t) \\ &\quad\quad + M_b^s(t) + \eta_b^s(t) \end{aligned} \tag{8}$$

where $\delta I^s(t) \doteq I^s(t) - \hat{I}^s(t)$. The first line of eqn. (8) contains the desired signal for the corrections. These signals have very small changes in rate over long periods of time (i.e., many minutes). The second line of eqn. (8) contains the noncommon-mode errors. These errors change rapidly and are zero mean over several minutes. Therefore, to also attain the ability to predict corrections at future times, the form of low pass filter that we select is line fitting to $\tilde{d}^s(t)$.

At time t_0, the line $a_{t_0} + b_{t_0}(t - t_0)$ is fit to the data

$$\left\{ \tilde{d}(\tau) \text{ for } \tau \in [t_0 - L, t_0] \right\}.$$

The parameters $[a_{t_0}, b_{t_0}, t_0, IODE]$ are communicated to the rover arriving at the rover at some time after t_0. The parameter $IODE$ ensures that the base and rover use the same issue of ephemeris data. For any time $t \geq t_0$, the rover computes the correction as

$$\hat{c}(t; t_0) = a_{t_0} + b_{t_0}(t - t_0) + \hat{I}^s(t). \tag{9}$$

For position computations, the rover uses the DGNSS compensated pseudorange measurement:

$$\Delta\rho_r^s(t; t_0) = \rho_r^s(t) - \hat{c}(t; t_0). \tag{10}$$

The correction latency is $l = (t - t_0)$. Assuming perfect cancellation of common-mode errors when $l = 0$ and elimination of the base multipath and receiver noise from the corrections, the DGNSS compensated pseudorange model is

$$\begin{aligned} \Delta\rho_r^s(t; t_0) \quad &\doteq \quad R(p_r(t), \hat{p}^s(t)) + (\hat{c}(t; t) - \hat{c}(t; t_0)) \\ &\quad\quad + M_r^s(t) + \eta_r^s(t). \end{aligned} \tag{11}$$

The term $(\hat{c}(t; t) - \hat{c}(t; t_0))$ accounts for the error in prediction of the common-mode errors due to communication latency.

Figures showing the results of example base station calculations are included in Appendix A. The differential correction in eqn. (9) is designed to be robust to latency and base station multipath error. Latency effects on both correction and positioning error are analyzed in Section VI.

The dominant error source in $\Delta\rho_r^s(t; t_0)$ is the rover multipath M_r^s which can be of several meters in magnitude. Addressing this rover multipath is necessary to achieve meter level performance. This issue is studied in Section V-B. The predictions of this study are verified experimentally in the results of Algorithm 3 in Section VI.

V. Position Estimation

This section considers the problem of position estimation from GNSS data. For this portion of the study a main question is position estimation sensitivity to correction latency.

The experimental analysis of position accuracy will use two position estimation algorithms: the linear Kalman filter [21], [41] and the risk-averse performance-specified approach [2], [42]–[44]. Each will be designed using a position, velocity, acceleration (PVA) state space model [21], [41] as outlined in Section V-A. The main applications of interest are moving vehicles. This portion of the study will only consider data from a stationary receiver, but the algorithms will be designed and tuned to be applicable to a moving vehicle. Section V-B considers a simplified system to highlight challenges related to and approaches for addressing multipath.

A. System Model

The state estimation algorithms (e.g., Kalman filter, RAPS) are designed using the standard state-space model:

$$x_{k+1} \quad \doteq \quad \phi x_k + \Gamma w_k \tag{12}$$

$$z_k \quad \doteq \quad H x_k + \eta_k. \tag{13}$$

The rover state vector is

$$x = [p^T, v^T, a^T, t_r, b_r, M]^T \in \mathbb{R}^{n_s}. \tag{14}$$

In (14) the symbols $p, v, a \in \mathbb{R}^3$ represent the rover position, velocity and acceleration, t_r and b_r are the receiver clock bias and drift, and $M \in \mathbb{R}^m$ represents the multipath error state vector. Therefore, $n_s = 11 + m$, where m is the number of available satellite measurements. The details of the state-space model, defining ϕ, Γ, $cov(w_k)$, and $cov(\eta_k)$ are described in Appendix B.

When both pseudorange and Doppler measurements are used, the observation matrix H is

$$H = \begin{bmatrix} \widehat{h}_{m\times 3} & 0_{m\times 3} & 0_{m\times 3} & 1_m & 0_m & I_{m\times m} \\ 0_{m\times 3} & \widehat{h}_{m\times 3} & 0_{m\times 3} & 0_m & 1_m & 0_{m\times m} \end{bmatrix}, \tag{15}$$

Copyright ©2018, University of California, Riverside. All Rights reserved.

where $\widehat{h}_m = [h^1 \;\; h^2 \ldots h^m]^T$ and each h^s is calculated using eqn. (4) at the computed values: $\hat{P}_r$ and $\hat{P}^s$. The symbol $I_{q\times q}$ represents the identity matrix with q rows and columns and $0_{a\times b}$ is the zero matrix with a rows and b columns. When only pseudorange is used, then the second set of rows is eliminated.

B. Simplified Illustrative Example

This section uses a simplified example to clarify the observability challenges connected to multipath and position estimation. It also clarifies the importance and use of the Doppler measurement to enhance the ability to attenuate the effects of multipath on the position estimates.

Simplified System. Consider the following 1-dimensional system with a standard position, velocity and acceleration (PVA) model. For this simplified case, the rover state vector is $x = [p, v, a, M]^T \in \mathbb{R}^4$ with $p, v, a \in \mathbb{R}$ being the rover position, velocity and acceleration and $M \in \mathbb{R}$ represents a multipath state. The receiver clock bias and drift t_r and b_r are neglected. The measurement white noise $\eta_k \sim \mathcal{N}(0, \sigma_\rho^2)$ has $\sigma_\rho = 0.5$ m, and

$$\phi = \begin{bmatrix} I & T & a_3 & 0 \\ 0 & I & a_2 & 0 \\ 0 & 0 & a_1 & 0 \\ 0 & 0 & 0 & \gamma_M \end{bmatrix} \text{ and } \Gamma = \begin{bmatrix} T^{5/2}/\sqrt{20} & 0 \\ T^{3/2}/\sqrt{3} & 0 \\ \sqrt{T} & 0 \\ 0 & \sqrt{T} \end{bmatrix}.$$

The process white measurement noise $w_k \sim \mathcal{N}(0, Q_d)$ with $Q_d \approx \begin{bmatrix} \sigma_a & 0 \\ 0 & \sigma_M \end{bmatrix}$. For Scenarios 1 and 2, the actual measurement matrix is $H = [1, 0, 0, 1]$. The remaining parameter values are stated in Appendix B.

Design Scenario 1: In this scenario, the designer makes the naive decision to design the estimator ignoring the multipath state, defining the estimator state as $\hat{x} = [p, v, a]^\top$ with $H = [1, 0, 0]$, and defining $R = 0.25 = \sigma_\rho^2$. Assuming that the actual state vector is defined to be the same as $\hat{x}$ (i.e., only the PVA states), the designer (optimistically) predicts the steady-state performance as indicated by the blue curve in Fig. 1.[1] When the designer tests the system in the real world (i.e., four states), the observed performance is indicated by the green curve in Fig. 1. The predicted performance is not achieved as the designer has neglected to account for the multipath state.

Design Scenario 2: Disappointed with the results of Scenario 1 and realizing the culprit is multipath error, the designer decides to continue with the same three state model, but to increase $R = 4.25m^2 = \sigma_\rho^2 + \gamma_m^2$, where $\gamma_m = (2m)^2$ is the covariance of the multipath error on the pseudorange. The designer (optimistically) predicts the performance as indicated by the red curve in Fig. 1. When the designer tests the system in the real world (i.e., four states) the observed performance is as indicated by the black curve in Fig. 1. The predicted is better (in the sense of being closer to the actual), but is still too conservative. The predicted and actual performance do not match because the design model is assuming that the multipath error is white, while for the actual system the multipath error is correlated in time. Also, the actual performance is only achieving meter-level accuracy at 63%.

[1]Performance is predicted by (1) computing the steady-state Kalman gain for the design model, (2) using that gain to compute the steady-state covariance of the actual system, (3) extracting the position error standard deviation, and (4) ploting the corresponding folded normal distribution. For additional detail on the analysis approach see Ch. 6 in [21].

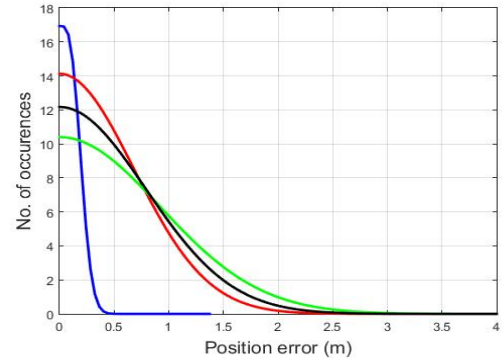

Fig. 1: Position error distribution for scenarios 1 and 2.

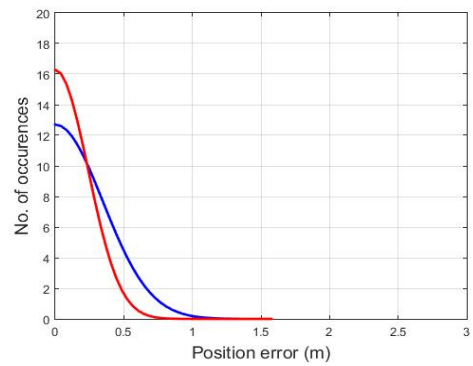

Fig. 2: Position error distribution for scenario 3 and 4

Design Scenario 3: This scenario uses the four state model in the design (i.e., including the multipath state). The measurement noise is assumed to be white noise with $R = 0.25 = \sigma_\rho^2$. With the four state model, the estimator accounts for the fact that there are correlated measurement errors (i.e., multipath) present and optimizes the estimator gain for the scenario.

Because the design and actual models are the same, their performance will match. This performance is shown by the blue curve in Fig. 2. The performance is not as good as that predicted for either of the design models in Fig. 1; however, it makes the correct prediction of the performance and its actual performance is better that either of the actual performances in Fig. 1. This design achieves meter-level accuracy at 88%.

Design Scenario 4: The system uses both the pseudorange and Doppler measurements. The measurement vector, H matrix, and measurement covariance matrix are:

$$z = \begin{bmatrix} \Delta\rho_r \\ \lambda D_r \end{bmatrix}, \quad H = \begin{bmatrix} 1 & 0 & 0 & 1 \\ 0 & 1 & 0 & 0 \end{bmatrix}, \quad R = \begin{bmatrix} \sigma_\rho^2 & 0 \\ 0 & \sigma_d^2 \end{bmatrix}$$

with $\sigma_d = 0.04$ m.

The estimator performance is shown by the red curve in Fig. 2. The performance is better than that for Scenario 3. This

Copyright ©2018, University of California, Riverside. All Rights reserved.

result should be obvious, as more information has been used to generate the estimate in Scenario 4; however, the specific contribution of the information is interesting. In Scenario 3, while the state is observable, the position and multipath are not highly separable. Adding the Doppler measurement in Scenario 4 directly measures the velocity, which greatly enhances the ability of the state estimator to seperably estimate p and M. The condition number of the observability matrix for Scenario 3 is more than 50000 times that of Scenario 4. This design achieves meter-level accuracy at 98%.

VI. Experimental Results: Latency Effects

This section presents results analyzing experimental performance. The analysis considers the effect of latency on the correction accuracy, the effect of latency on position estimation accuracy, and the extent to which of different Kalman filter based estimation algorithms are able to achieve the one-meter accuracy specification. These results were first reported in [1].

A. Experimental Data Description

The experimental data was acquired using a consumer-grade, single-frequency GNSS receiver (u-blox M8T). The duration of the experiment is 3000 seconds. All data is saved and post-processed so that multiple algorithms can be compared using identical data. All results are produced using only pseudorange and Doppler data. Phase measurements were not considered.

The base station data was obtained using the RTCM standard [11] and NTRIP protocol from two base stations: ESRI (baseline separation 14.5 km) and UCR (baseline separation 6 m). The DGNSS correction parameters $[a_{t_0}, b_{t_0}, t_0, IODE]$ are computed and stored (using $L = 500$). This value of L was selected to be about four times the expected base multipath correlation time. The DGNSS corrections $c(t;t-\ell)$ will be used at time t to study the impact of the latency ℓ.

All the results shown in this section are conducted for a stationary rover with the GNSS receiver connected to an antenna at a surveyed location. The stationary rover state estimation algorithm has parameters tuned for a rover that is in motion (i.e., not stationary).

B. Correction Sensitivity to Latency

The correction error due to communication latency, as defined in eqn. (11) is

$$e_c(k,l) = |\hat{c}(k;k) - \hat{c}(k;k-l)|, \tag{16}$$

where $\hat{c}(k;k)$ is the correction with no latency and $\hat{c}(k;k-l)$ is the correction with latency of l epochs, where both corrections are computed using eqn. (9).

Fig. 3 shows the mean plus and minus the standard deviation of $e_c(k,l)$ as a function of l for three satellites. For each fixed value of l and each satellite, the mean and standard deviation of $e_c(k,l)$ are computed from experimental data by averaging over $(3000-l)$ epochs.

The correction error $e_c(k,l)$ remains less than one meter for up to 600 seconds.

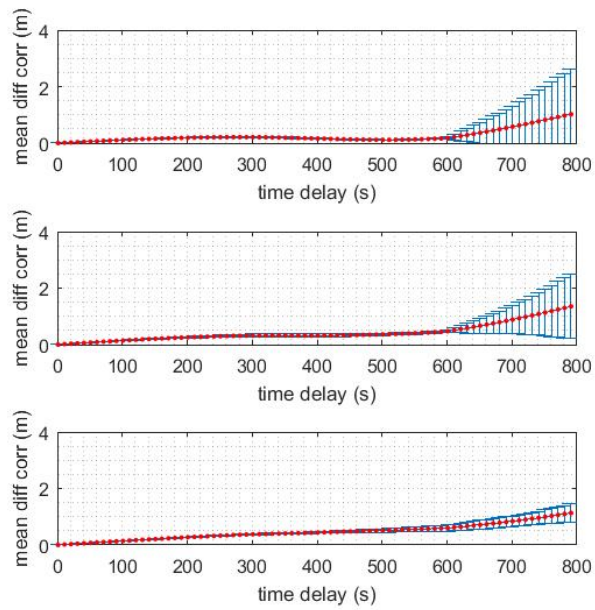

Fig. 3: Correction error defined in eqn. (16) versus latency for three satellites.

C. Position Estimation Algorithms

The following subsections report positioning accuracy experimental results for 3 estimation algorithms:

1) an 11 state Kalman Filter (KF) with state defined as $x(t) = [p^T, v^T, a^T, t_r, d_r]^T$ using only pseudorange measurements;
2) an $(11+m)$ state KF with the state defined in eqn. (14) using only pseudorange measurements; and,
3) an $(11+m)$ state KF with the state defined in eqn. (14) with pseudorange and Doppler measurements.

All the Kalman filter implementations use a PVA model [21], [41]. Additional details are included in Section V-A and Appendix B. Each algorithm is used to process the entire set of measurements ($k = 1,\ldots,3000$ seconds) as if they were occurring in real-time (i.e., incrementally) to estimate the state vector at each time k, using correction $\hat{c}(k;k-l)$ from eqn. (9) for a given value of the latency l. For algorithm n and latency l, this produces the position sequence $\hat{p}^n_{k,l}$. The experiment is repeated for each algorithm for latency values $l = 0,\ldots,900$ seconds.

The norm of horizontal position error is

$$e^n_{h_{k,l}} = \|p_r - \hat{p}^n_{k,l}\| \tag{17}$$

where p_r is the known antenna position and $\hat{p}^n_{k,l}$ is the estimated position for algorithm n, time epoch k, and correction latency l.

D. Positioning Accuracy

Fig. 4(a-c) show histograms of the norm of horizontal position error $e^n_{h_{k,l}}$ defined in eqn. (17) for latency $l = 0$ for each algorithm as summarized in Section VI-C.

Copyright ©2018, University of California, Riverside. All Rights reserved.

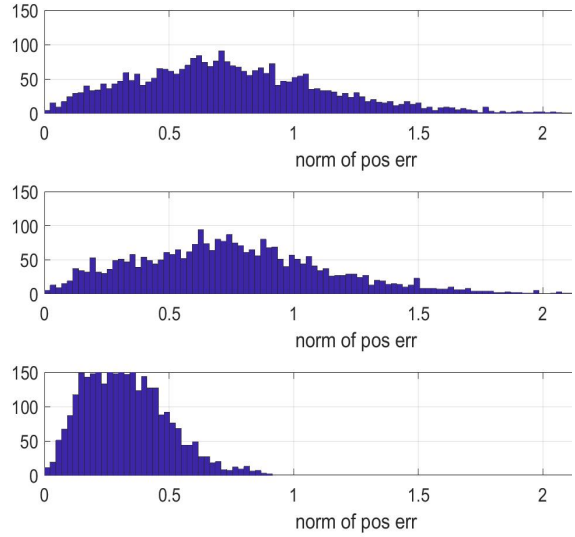

Fig. 4: Histogram of the horizontal position error $e^n_{h_{k,l}}$ defined in eqn. (17) for Algorithm 1 (Top), Algorithm 2 (Middle), Algorithm 3 (Bottom) with $l = 0$.

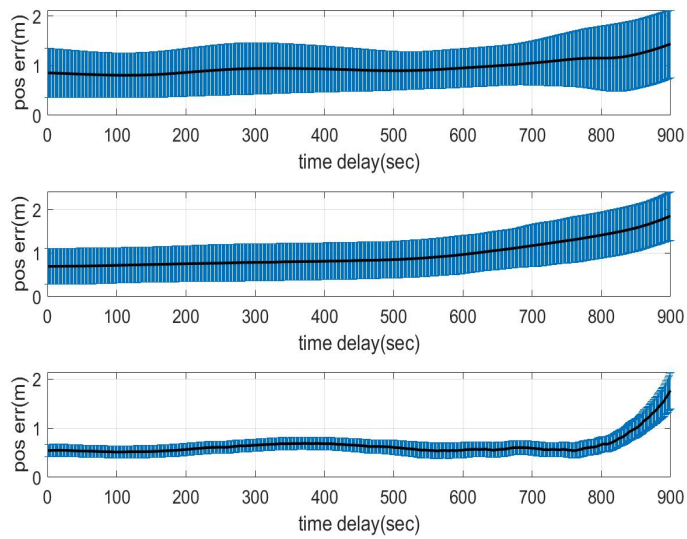

Fig. 5: Horizontal position error vs latency. Algorithm 1 (Top). Algorithm 2 (Middle). Algorithm 3 (Bottom).

TABLE I: Horizontal Positioning Performance with $l = 0$.

Algo.	Mean	Std. Dev	Max	Prob.	
				$e_h < 1$	$e_h < 2$
1	0.74	0.38	2.25	76	99.6
2	0.75	0.38	2.28	76	99.6
3	0.33	0.16	0.91	100	100

Table I and II summarize various measures of positioning accuracy when the latency is zero. Horizontal position error e_h is in Table I. Vertical error e_v is in Table II. Column 1 shows the algorithm number. Column 2 displays the mean error. Column 3 contains the error standard deviation. Column 4 shows the maximum value of the position error. Columns 5 and 6 report the percentage of the samples that have a error less than 1.0 and 2.0 meters, respectively.

Fig. 4, Table I and Table II demonstrate that including the multipath state vector and using the Doppler measurement significantly improves the performance in all standard, as was motivated by the simplified examples in Section V-B.

E. Positioning Sensitivity to Latency

For each of the three algorithms described in Section VI-C, Fig. 5 illustrates the effect of the DGNSS correction latency l on GNSS position accuracy as measured by $e^n_{h_{k,l}}$ defined in eqn. (17). In each graph, the black curve shows the mean of $e^n_{h_{k,l}}$. Each point on the graph is also marked with a one-standard-deviation error bar that is indicated in blue.

Fig. 5 shows that position estimation accuracy is insensitive to communication latency for delays up to 600 sec.

TABLE II: Vertical Positioning Performance with $l = 0$.

Algo.	Mean	Std. Dev	Max	Prob.	
				$e_v < 2$	$e_v < 3$
1	0.76	0.62	3.6	95	99.7
2	0.76	0.68	3.5	95	99.6
3	0.59	0.38	1.65	100	100

VII. Experimental Results: Position Accuracy with Outliers

This section discusses achievable performance and the effects of outliers using the first 1000 seconds of data described in Section VI-A. These results were first reported in [2].

A. Outlier Generation

Due to the location of the stationary antenna on the roof of a four story building, the sky was clear and there were no obstacles; therefore the collected data set should contained no outliers. This was confirmed by analysis of the KF residuals.

To allow analysis of algorithm performance in the presence of outliers, outliers were added to the pseudorange measurements in a sequence of Monte Carlo tests. For each Monte Carlo test, computer-generated outliers are added to two randomly chosen measurements at each time instant. The size of each outlier is drawn from a uniform distribution parameterized by $\mu \in [0.2, 20]$. For $\mu < 4$, the distribution is $U[0, \mu + 4]$. For $\mu >= 4$, the distribution is $U[\mu - 4, \mu + 4]$. For each Monte Carlo run, the same outlier corrupted data is used for all algorithms.

B. State Space Model

All analysis in this section uses the PVA model as defined in Section V-A and Appendix B. The state vector is defined in eqn. (14). Both pseudorange and Doppler measurements are used. The H matrix is defined by eqn. (15).

Copyright ©2018, University of California, Riverside. All Rights reserved.

C. State Estimation Algorithms

This section compares the results of three algorithms:

- **Kalman filter (KF)**: This is Algorithm 3 defined in Section VI-C. This algorithm uses all measurements and no outliers are added. These results show the best possible results in an ideal outlier-free situation.
- **Neyman-Pearson Kalman filter (NP-KF)**: This is Algorithm 3 defined in Section VI-C except that measurements are only used if they pass a Neyman-Pearson check on the absolute value of their residual. This algorithm has all the measurements available to it, but outliers have been added as described in Section VII-A. The NP-KF ignores all measurements for which the absolute value of their residual is greater than the threshold $s_{ii} = \gamma\sqrt{R_{ii} + h_i P_k^- h_i^\top}$ where h_i is the ith row of H and γ is a positive constant. Unless otherwise stated, the results herein use $\gamma = 5$.
- **Risk-Averse Performance-Specified (RAPS)**: The RAPS approach is discussed briefly in Appendix C. The measurements to be used at each epoch are selected based on risk minimization subject to a constraint on the expected accuracy. The measurement update for the selected measurements is the same as for a Kalman filter. This algorithm has all the measurements available to it, but outliers have been added as described in Section VII-A.

These algorithms will all use the same data, with the same outlier corruption, and performance is compared.

D. Performance Metrics

Peformance analysis will compare the norm of the horizontal position error, sub-meter accuracy percentage, and maximum position error. The norm of the horizontal position error is calculated as:

$$E_{p_k}^n = \|p_r - \hat{p}_k^n\| \tag{18}$$

where p_r is the surveyed antenna position, $\hat{p}_k^n$ is the estimated rover position at time epoch k. The symbol n is the algorithm number.

E. Experimental Results: Single Run

Fig. 6 compares the position error for the three algorithms using two different values of the outlier parameter μ. This is one example simulation of the Monte Carlo analysis that will follow. The blue curve is the KF without outliers, representing the best performance achievable for the given dataset. The red and green curves represent the performance of RAPS and NP-KF when outliers are added. In top set of graphs the outlier parameter is $\mu = 8$. In the bottom set of graphs the outlier parameter is $\mu = 13$. In both figures, the RAPS performance with outliers is not quite as good as the KF (no outliers), but better than NP-KF with outliers. The performance of the NP-KF is improved in the bottom graph ($\mu = 13$) relative to that in the top graph ($\mu = 13$), because the larger magnitude of the outlier results in the threshold test being more successful in correctly detecting and removing outliers.

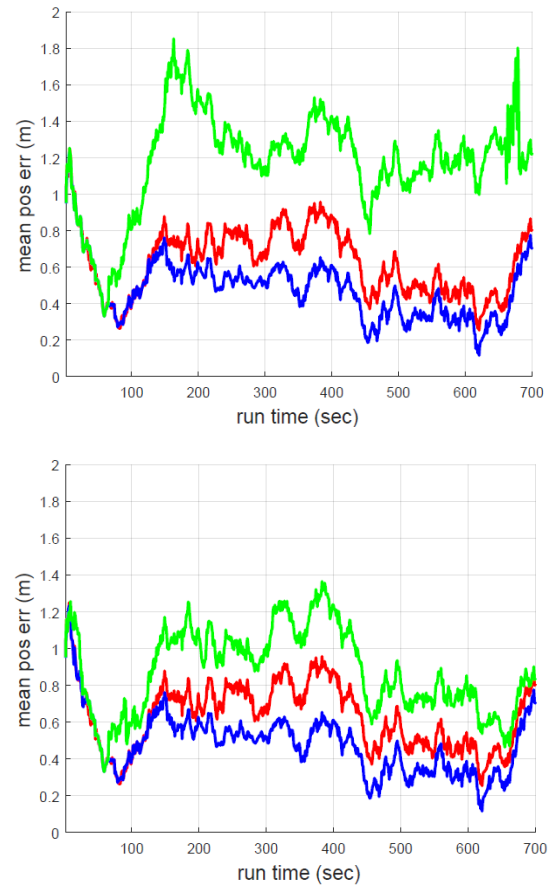

Fig. 6: Performance Comparison. Blue curves are the Kalman Filter without outliers. Green curves are for NP-KF with outliers. Red curves are for RAPS with outliers. Top has $\mu = 8$; Bottom has $\mu = 13$.

It is important to note that the RAPS approach does not simply use the smallest residuals. Selecting the smallest residuals might not satisfy the performance constraint, because the corresponding rows of the H matrix may not be sufficiently diverse. In the RAPS approach, the optimization process ensures that the selected measurements result in sufficient diversity in the rows of H to satisfy the position error specification, while minimizing the risk of including outliers. As the number of measurements that are used increases, the expected information from those measurement increases, but so does the risk of inclusion of outliers. RAPS may ignore some of the smaller residuals, as they would add risk without supplying a sufficient amount of new information. In the RAPS approach the number of measurements used at each time may vary. In this experiment, over 60% of the measurements at each time are used.

Table III summarizes various measures of positioning accuracy for $[0, 1000]$ seconds of data with two different scenarios: *a*) The outlier magnitude is $\mu = 8$. The results are presented in the column headed by *NP-KF1*. *b*) The outlier magnitude is $\mu = 13$. The results are presented in the column headed by *NP-KF2*. The RAPS results for the two scenarios were the same to within centimeters of accuracy.

Copyright ©2018, University of California, Riverside. All Rights reserved.

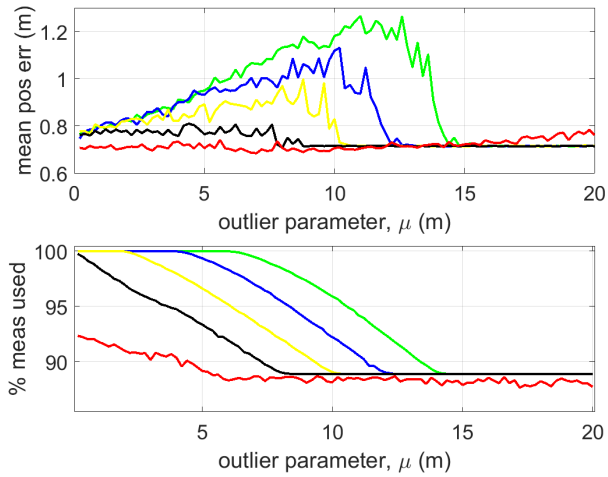

Fig. 7: (Top) Position error and (Bottom) Percentage of used measurement versus outlier magnitude. Red curves are for RAPS. Black, yellow, blue and green are for NP-KF with $\gamma = 2, 3, 4$ and 5.

TABLE III: Algorithm Comparison. The KF is outlier free. NP-KF and RAPS have outliers.

Performance analysis	KF	NP-KF1	NP-KF2	RAPS
Mean of position error (m)	0.55	1.17	0.85	0.59
Std. of position error (m)	0.17	0.28	0.26	0.18
Sub-meter accuracy %	99	19	67	98
Maximum error (m)	1.2	1.8	1.4	1.2
Outlier parameter, μ (m)	0	8	13	8, 13

The first and second rows of the table compare the mean and standard deviation (std) of horizontal position error defined in eqn. (18). Row 3 reports the percentage of samples that achieved sub-meter accuracy. Without outliers, the KF demonstrates 99% of samples achieving submeter accuracy. With outliers, the RAPS approach achieves 98% of the samples with submeter accuracy. The NP-KF approach achieves lower percentages with submeter accuracy. Its performance would be altered by selecting different values for the threshold test parameter γ.

F. Experimental Results: Monte Carlo

Fig. 7 shows the NP-KF and RAPS performance, averaged over 20 Monte Carlo simulations. To produce one point on each curve for one value of $\mu \in [0.2, 20]$ meter: (1) twenty experiments were performed over $[0, 1000]$ seconds; (2) the position error at each second was computed; (3) the position error was averaged both over the 1000 seconds and the 20 Monte Carlo experiments. Each Monte Carlo experiment generate a different set of outliers that was used both for NP-KF and RAPS. With nine satellites available and two outliers per epoch, the measurement set (pseudorange plus Doppler) contains 11% outliers. The red curves display the result for the RAPS algorithm. The other curves display the results for the NP-KF approach for different values of the threshold parameter γ. The black, yellow, blue, and green curves correspond to γ values of 2, 3, 4, and 5, respectively. The y-axis in the top figure is the mean position error. The y-axis in bottom figure is the percentage of the measurements that were used for state estimation. NP-KF uses all measurements when μ is small. Then its threshold test removes an increasingly higher percentage of the outliers as the magnitude of the outlier increases, until it is correctly removing 11% of the measurements. Therefore, NP-KF mean error initially rises and later falls as the magnitude of the outlier increases. RAPS mean position error performance is robust to the magnitude of the outlier.

VIII. Conclusion and Future Work

Real-time absolute positioning (i.e., relative to an Earth frame) is one of the primary requirements of navigation technology in important commercial applications, e.g. connected and autonomous vehicles. Data communication latency, interruption, and lost packets are the challenges that all real-time systems encounter. Reliably achieving submeter position accuracy in realistic environments is a main focus of this research project.

This report discussed GNSS measurement error characteristics and methods to accommodate them. The report provides an algorithm able to compensate latency, short-term communication interruption, and lost packets. The prime contributions of the research described in this report are [1], [2]: (1) demonstrating that, with suitable algorithmic processing, positioning performance is insensitive to correction latency up to 600 s; and (2) demonstating that horizontal position estimation accuracy at the submeter level for over 99% of samples.

Future research will focus on extending the results herein to vehicle positioning performance on maneuvering platforms, real-time implementations, and the use of inertial navigation [21], [45], [46]; inclusion of carrier phase measurements [21], multiple frequencies (L2, L5), and multiple constellations (e.g., Galileo, BeiDou, QZSS, IRNSS) [47]–[50] for achieving precise positioning could be another research motivation.

IX. Acknowledgement

This work was partially supported by Sirius XM. We gratefully acknowledge this support. All opinions expressed in this article are those of the authors.

References

[1] F. Rahman, E. Aghapour, and J. A. Farrell, "ECEF Position Accuracy and Reliability in the Presence of Differential Correction Latency," *Proc. of IEEE/ION PLANS, in press*, 2018.

[2] E. Aghapour, F. Rahman, and J. A. Farrell, "Risk-averse performance-specified state estimation," *Proc. of IEEE/ION PLANS, in press*, 2018.

[3] P. Misra and P. Enge, "Special issue on global positioning system," *Proc. of the IEEE*, vol. 87, no. 1, pp. 3–15, 1999.

[4] B. Hofmann-Wellenhof, H. Lichtenegger, and J. Collins, *"Global Positioning System: Theory and Practice"*. Springer Science & Business Media, 2012.

[5] G. Blewitt, "Basics of the GPS Technique: Observation Equations," *Geodetic applications of GNSS*, pp. 10–54, 1997.

[6] C. Shuxin, Y. Wang, and C. Fei, "A study of differential GNSS positioning accuracy," *in 3rd Int. Conf. on Microwave and Millimeter Wave Tech.*, pp. 361–364, 2002.

Copyright ©2018, University of California, Riverside. All Rights reserved.

[7] S. Johnson, L. Rolfes *et al.*, "Connected Vehicle Pilot Deployment Program Phase II Data Privacy Plan-Tampa (THEA)." USDOT, Tech. Rep., February, 2017. [Online]. Available: https://rosap.ntl.bts.gov/view/dot/32763

[8] S. Cadzow *et al.*, "Connected Vehicle Pilot Deployment Program Phase 2: Data Privacy Plan-New York City." USDOT, Tech. Rep., December, 2016. [Online]. Available: https://rosap.ntl.bts.gov/view/dot/32311

[9] F. M. Kitchener, T. English *et al.*, "Connected Vehicle Pilot Deployment Program Phase 2, Data Management Plan-Wyoming." USDOT, Tech. Rep., April, 2017. [Online]. Available: https://transportationops.org/publications/connected-vehicle-pilot-deployment-program-phase-2-data-management-plan-wyoming-dot

[10] P. Teunissen and O. Montenbruck, *Handbook of Global Navigation Satellite Systems*. Springer, 2017, vol. 26(2).

[11] Anonymous, "RTCM Standard 10403.2 for Differential GNSS (Global Navigation Satellite Systems) Services," RTCM Special Committee, Tech. Rep., August, 2001.

[12] P. K. Enge, R. M. Kalafus, and M. F. Ruane, "Differential operation of the global positioning system," *IEEE Comm. Mag.*, vol. 26(7), pp. 48–60, 1988.

[13] P. Teunissen, "Differential GPS: Concepts and Quality Control," *Netherlands Institution of Navigation, Amsterdam*, 1991.

[14] J. A. Farrell, M. Grewal, M. Djodot, and M.Barth, "Differential GNSS with latency compensation for autonomous navigation," *Int. Symp. on Int. Cont.*, pp. 20–24, 1996.

[15] J. A. Farrell, M. Djodat, M. Barth, and M. Grewal, "Latency compensation for differential GPS," *Navigation*, vol. 44(1), pp. 99–107, 1997.

[16] M. S. Braasch and A. Van Dierendonck, "GPS receiver architectures and measurements," *Proc. of the IEEE*, vol. 87(1), pp. 48–64, 1999.

[17] M. S. Grewal, L. R. Weill, and A. P. Andrews, *"Global Positioning System, Inertial Navigation,and Integration"*. John Wiley & Sons, 2007.

[18] P. Misra and P. Enge, "Global Positioning System: Signals, Measurements and Performance, second edition," *Massachusetts: Ganga-Jamuna Press*, 2006.

[19] B. W. Parkinson, J. Spilker, and P. Enge, "Global Positioning System: Theory and Applications," *AIAA*, vol. 2, pp. 3–50, 1996.

[20] P. Enge, "The global positioning system: Signals, measurements, and performance," *Int. J. of Wireless Info. Net.*, vol. 1(2), pp. 83–105, 1994.

[21] J. A. Farrell, *"Aided Navigation: GNSS with High Rate Sensors"*. McGraw-Hill Inc, 2008.

[22] G. Wübbena, A. Bagge, G. Seeber, V. Böder, P. Hankemeier *et al.*, "Reducing distance dependent errors for real-time precise DGPS applications by establishing reference station networks," *Proc. OF ION GPS*, vol. 9, pp. 1845–1852, 1996.

[23] C. Kee, B. W. Parkinson, and P. Axelrad, "Wide area differential GPS," *Navigation*, vol. 38(2), pp. 123–145, 1991.

[24] P. Enge, T. Walter, S. Pullen, C. Kee, Y.-C. Chao, and Y.-J. Tsai, "Wide area augmentation of the global positioning system," *Proc. of the IEEE*, vol. 84(8), pp. 1063–1088, 1996.

[25] L. Dai, S. Han, J. Wang, and C. Rizos, "A study on GPS/GLONASS multiple reference station techniques for precise real-time carrier phase-based positioning," *Proc. of ION GPS*, pp. 392–403, 2001.

[26] P. Loomis, G. Kremer, and J. Reynolds, "Correction algorithms for differential GPS reference stations," *Navigation*, vol. 36(2), pp. 179–193, 1989.

[27] G. T. Kremer, R. M. Kalafus, P. V. Loomis, and J. C. Reynolds, "The effect of selective availability on differential GPS corrections," *Navigation*, vol. 37, no. 1, pp. 39–52, 1990.

[28] Y. Saber, R. Antri-Bouzar, M. Sebeloue, and J. Boucher, "Comparison between two navigation modes for differential GPS," *Proc. of IEEE Microwave and Millimeter Wave Tech. Conf.*, pp. 463–466, 1998.

[29] B. Park, J. Kim, and C. Kee, "RRC unnecessary for DGPS messages," *IEEE T. on Aero. and Elec. Sys.*, vol. 42(3), 2006.

[30] B. Townsend and P. Fenton, "A practical approach to the reduction of pseudorange multipath errors in a L1 GPS receiver," *Proc. of the 7th Int. Tech. Meeting of the Sat. Div. of the ION*, 1994.

[31] F. Lee, S. Chun, Y. J. Lee, T. Kang, G. Jee, and J. Kim, "Parameter estimation for multipath error in GPS dual frequency carrier phase measurements using unscented Kalman filters," *Int. J. of Cont., Auto., and Sys.*, vol. 5(4), pp. 388–396, 2007.

[32] J. K. Ray, *"Mitigation of GPS Code and Carrier Phase Multipath Effects Using a Multi-Antenna System"*. University of Calgary, 2000.

[33] J. M. Tranquilla, J. Carr, and H. M. Al-Rizzo, "Analysis of a choke ring groundplane for multipath control in global positioning system (GPS) applications," *IEEE T. on Ant. and Prop.*, vol. 42(7), pp. 905–911, 1994.

[34] L. Serrano, D. Kim, R. B. Langley, K. Itani, and M. Ueno, "A GPS velocity sensor: how accurate can it be?–a first look," *ION NTM*, vol. 2004, pp. 875–885, 2004.

[35] L. Serrano, D. Kim, and R. B. Langley, "A single GPS receiver as a real-time, accurate velocity and acceleration sensor," *Proc. of the 17th Int. Tech. Meeting of the Sat. Div. of ION*, vol. 2124, 2004.

[36] M. D. Agostino, A. Manzino, and G. Marucco, "Doppler measurement integration for kinematic real-time GPS positioning," *Applied Geomatics*, vol. 2(4), pp. 155–162, 2010.

[37] J. An and J. Lee, "Improvement of GPS position estimation using SNR and Doppler," *in IEEE Int. Conf. on AIM*, pp. 1645–1650, 2017.

[38] G. Lachapelle, "GNSS observables and error sources for kinematic positioning," *Kinematic Systems in Geodesy, Surveying, and Remote Sensing*, pp. 17–26, 1991.

[39] J. Zumberge, M. Heflin, D. Jefferson, M. Watkins, and F. H. Webb, "Precise point positioning for the efficient and robust analysis of gps data from large networks," *Journal of geophysical research: solid earth*, vol. 102(B3), pp. 5005–5017, 1997.

[40] J. Kouba and P. Héroux, "Precise point positioning using igs orbit and clock products," *GPS solutions*, vol. 5(2), pp. 12–28, 2001.

[41] R. Brown and P. Hwang, *"Introduction to Random Signals and Applied Kalman Filtering"*. Wiley, New York, 1996.

[42] E. Aghapour and J. A. Farrell, "Performance specified state estimation with minimum risk," *American Control Conference*, 2018.

[43] ——, "Performance specified moving horizon state estimation with minimum risk," *ECC*, in press 2018.

[44] E. Aghapour, F. Rahman, and J. A. Farrell, "Outlier accommodation by risk-averse performance-specified linear state estimation," *Proc. of IEEE/CDC*, 2018.

[45] J. A. Farrell and P. F. Roysdon, "Advanced vehicle state estimation: A tutorial and comparative study," *IFAC-PapersOnLine*, vol. 50(1), pp. 15 971–15 976, 2017.

[46] H. Qi and J. B. Moore, "Direct Kalman filtering approach for GPS/INS integration," *IEEE Transactions on Aerospace and Electronic Systems*, vol. 38(2), pp. 687–693, 2002.

[47] R. Odolinski, P. Teunissen, and D. Odijk, "An analysis of combined COMPASS/BeiDou-2 and GPS single-and multiple-frequency RTK positioning," *Proc. of the ION Pacific PNT Meeting*, pp. 69–90, 2013.

[48] N. Nadarajah, A. Khodabandeh, and P. J. Teunissen, "Assessing the IRNSS L5-signal in combination with GPS, Galileo, and QZSS L5/E5a-signals for positioning and navigation," *GPS solutions*, vol. 20(2), pp. 289–297, 2016.

[49] D. Odijk, N. Nadarajah, S. Zaminpardaz, and P. J. Teunissen, "GPS, Galileo, QZSS and IRNSS differential ISBs: estimation and application," *GPS solutions*, vol. 21(2), pp. 439–450, 2017.

[50] M. Choi, J. Blanch, D. Akos, L. Heng, G. Gao, T. Walter, and P. Enge, "Demonstrations of multi-constellation advanced RAIM for vertical guidance using GPS and GLONASS signals," *Proc. of the ITM of the Satellite Division of the ION (ION GNSS 2011)*, pp. 3227–3234, 2011.

[51] J. Neyman and E. S. Pearson, "The testing of statistical hypotheses in relation to probabilities a priori," in *Mathematical Proceedings of the Cambridge Philosophical Society*, vol. 29, no. 4. Cambridge University Press, 1933, pp. 492–510.

[52] A. S. Willsky, "A survey of design methods for failure detection in dynamic systems," *Automatica*, pp. 601–611, 1976.

[53] E. Y. Chow and A. S. Willsky, "Issues in the development of a general design algorithm for reliable failure detection," *IEEE Conf. on Decision and Control*, pp. 1006–1012, 1980.

[54] E. Chow and A. Willsky, "Analytical redundancy and the design of robust failure detection systems," *IEEE Transactions on Automatic Control*, vol. 29, no. 7, pp. 603–614, 1984.

[55] R. A. Fisher, "Statistical methods for research workers," in *Breakthroughs in Statistics*. Springer, 1992, pp. 66–70.

[56] R. J. Patton and J. Chen, "Review of parity space approaches to fault diagnosis for aerospace systems," *Journal of guidance control and dynamics*, vol. 17, pp. 278–278, 1994.

[57] R. G. Brown, "A baseline GNSS RAIM scheme and a note on the equivalence of three RAIM methods," *Navigation*, vol. 39, no. 3, pp. 301–316, 1992.

Copyright ©2018, University of California, Riverside. All Rights reserved.

[58] ——, "Solution of the Two-Failure GPS RAIM Problem Under Worst-Case Bias Conditions: Parity Space Approach," *Navigation*, pp. 425–431, 1997.

[59] R. Brown and P. Hwang, "From RAIM to NIORAIM A New Integrity Approach to Integrated Multi-GNSS Systems," *Inside GNSS, May-June*, 2008.

[60] M. A. Sturza, "Navigation system integrity monitoring using redundant measurements," *Navigation*, vol. 35, no. 4, pp. 483–501, 1988.

[61] R. Patton, "Fault detection and diagnosis in aerospace systems using analytical redundancy," *Computing & Control Engineering Journal*, pp. 127–136, 1991.

[62] J. Angus, "RAIM with multiple faults," *Navigation*, pp. 249–257, 2006.

[63] S. Weisberg, *Applied linear regression*. John Wiley & Sons, 2005, vol. 528.

[64] S. Hewitson and J. Wang, "Extended receiver autonomous integrity monitoring (E RAIM) for gnss/ins integration," *Journal of Surveying Engineering*, vol. 136, pp. 13–22, 2010.

[65] L. Carlone, A. Censi, and F. Dellaert, "Selecting good measurements via l1 relaxation: A convex approach for robust estimation over graphs," in *IROS*. IEEE, 2014, pp. 2667–2674.

[66] J. Wright, A. Y. Yang, A. Ganesh, S. S. Sastry, and Y. Ma, "Robust face recognition via sparse representation," *IEEE transactions on pattern analysis and machine intelligence*, vol. 31, no. 2, pp. 210–227, 2009.

[67] X. Mei and H. Ling, "Robust visual tracking using l1 minimization," in *Computer Vision*. IEEE, 2009, pp. 1436–1443.

[68] D. Wang, H. Lu, and M.-H. Yang, "Robust visual tracking via least soft-threshold squares," *IEEE Transactions on Circuits and Systems for Video Technology*, vol. 26, pp. 1709–1721, 2016.

[69] P. Huber, *Robust Statistics*. New York, John Wiley and Sons Inc, 1981.

[70] A. M. Leroy and P. J. Rousseeuw, "Robust regression and outlier detection," *New York: Wiley, 1987*, 1987.

[71] S. Zhao, Y. Chen, H. Zhang, and J. A. Farrell, "Differential GPS aided inertial navigation: A contemplative realtime approach," *IFAC*, pp. 8959–8964, 2014.

[72] P. F. Roysdon and J. A. Farrell, "Robust GPS-INS Outlier Accommodation: A Soft-thresholded Optimal Estimator," *IFAC*, pp. 3574–3579, 2017.

APPENDIX

A. Example Computed Corrections

This section illustrates the DGNSS correction approach described in Section IV using an example set of data. The blue points in Fig. 8 show the DGNSS corrections $\tilde{c}$ as computed using eqn. (5). The model corresponding to $\tilde{c}$ is defined in eqn. (6). An estimate $\hat{I}^s(t)$ of the first term (i.e., $I^s(t)$) is computable from ionosphere model parameters communicated in the satellite data and is plotted as the green line in Fig. 8.

The blue curve in Fig. 9 is the ionospheric-free DGNSS correction, $\tilde{d}$, formed using eqn. (7) and has the model described in eqn. (8). While the slope of $\tilde{c}$ was approximately 3 mm/sec, the slope of $\tilde{d}$ is reduced to approximately 1.5 mm/sec.

Over long periods of time (e.g., hours), $\tilde{d}(t)$ will not be linear due to the rising and setting of the satellite causing the signal to traverse paths through different portions of the ionoshpere that vary in length and time of day. See Fig. 10. Alternative, over very short intervals of time, line fitting might fit either the random noise or multipath effects without providing useful predictive capability of future common-mode errors. For L greater than a few multiples of the multipath correlation time, multipath effects will be attenuated and the line fit should have useful predictive capabilities. In Fig. 11 the blue dots again show $\tilde{d}$. The red line shows the line fit to $\tilde{d}(t)$ for $t \in [t_0 - L, t_0]$ for $t_0 = 500$ and $L = 500$. On the interval $t \in [t_0 - L, t_0]$, the line follows the general trend of the data without following the random noise or multipath. For

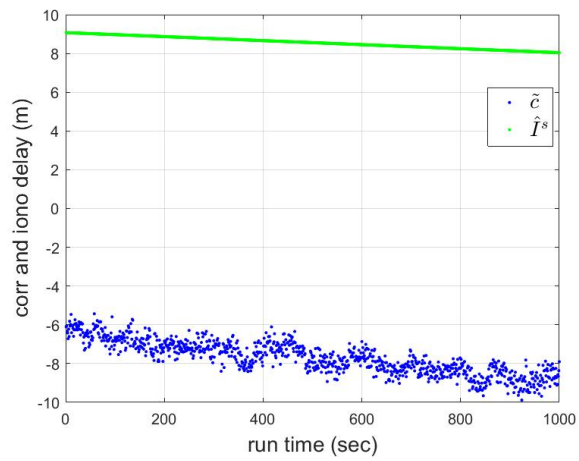

Fig. 8: DGNSS correction $\tilde{c}$ (blue) and computed ionospheric delay $\hat{I}^s(t)$ (green).

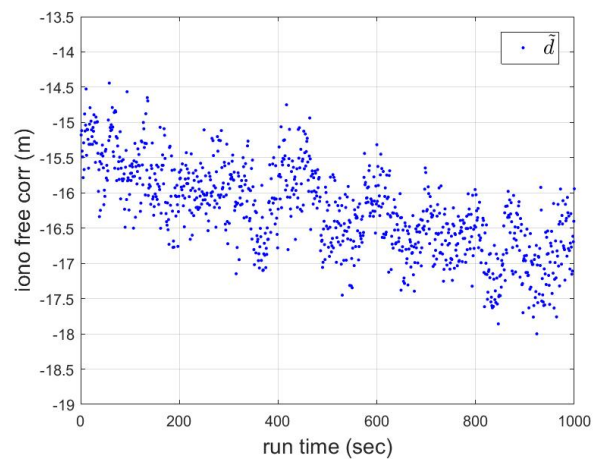

Fig. 9: Ionospheric-free correction $\tilde{d}(t)$.

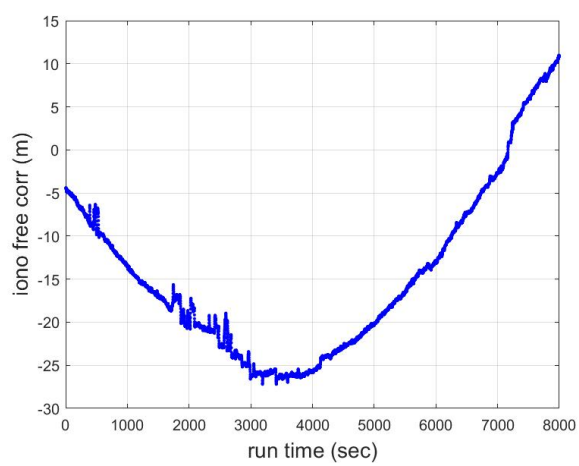

Fig. 10: Ionospheric-free correction $\tilde{d}(t)$ for long period of time

Copyright ©2018, University of California, Riverside. All Rights reserved.

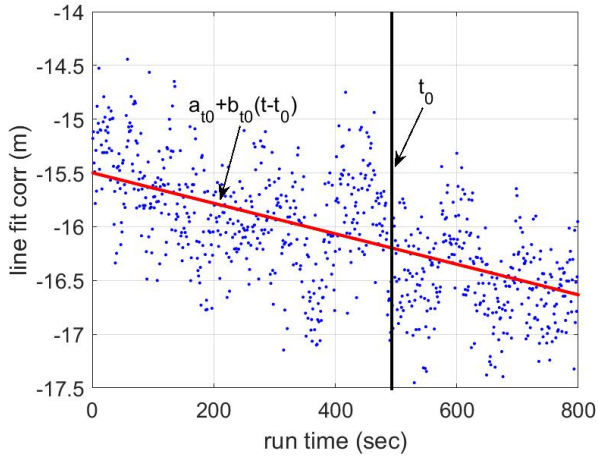

Fig. 11: Line fit to ionospheric delay free correction.

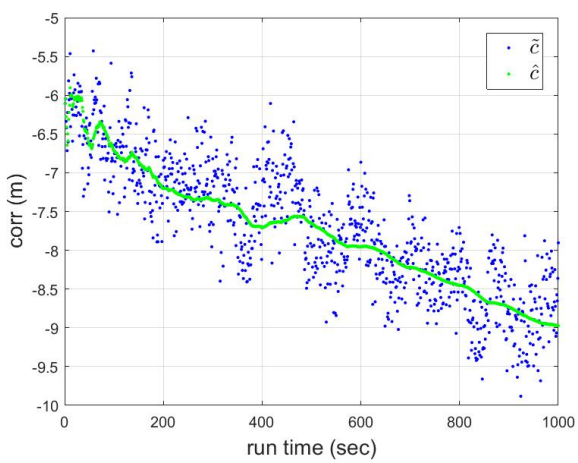

Fig. 12: DGNSS correction raw data $\tilde{c}$ and computed correction $\hat{c}(t;t)$.

$t > t_o$, the line fit predicts the general trend of $\tilde{d}(t)$. The prediction accuracy will decease (as expected) as $(t - t_0)$ increases. Fitting the line to $\tilde{d}$ provides the parameters t_0, a_{t0} and b_{t0}.

Finally, the correction $\hat{c}(t;t)$, as computed using eqn. (9), is shown as the green line in Fig. 12 along with the original data (blue dots).

B. Kalman Filter Design

The state space model has the standard form described in eqns. (12-13). The state vector defined in eqn. (14) has three vector sub-components: the vehicle state $x_v = [p^T, v^T, a^T]^T \in \mathbb{R}^9$, the clock state $x_c = [t_r, b_r]^T \in \mathbb{R}^2$, and the multipath state $M \in \mathbb{R}^m$, such that $x = [x_v^T, x_c^T, M^T]^T \in \mathbb{R}^{m+11}$. Each of these three sub-components evolve independently through time, which simplifies the definition of the state space model.

The matrices of the discrete-time state-space model are

$$\phi = \begin{bmatrix} \phi_v & 0 & 0 \\ 0 & \phi_c & 0 \\ 0 & 0 & \phi_M \end{bmatrix}, \quad \Gamma = \begin{bmatrix} \Gamma_v & 0 & 0 \\ 0 & \Gamma_c & 0 \\ 0 & 0 & \Gamma_M \end{bmatrix} \text{ and}$$

$$Q_d = \begin{bmatrix} Q_{d_v} & 0 & 0 \\ 0 & Q_{d_c} & 0 \\ 0 & 0 & Q_{d_M} \end{bmatrix}.$$

In the following definitions of the model portions, the time-step is defined as $T = 0.1$s. The GNSS epochs will occur at 1 Hz. Therefore, the time update will occur 10 times between measurement epochs. Alternatively, the analysis could have used $T = 1$ with a single time update between measurement epochs. The conclusions of the analysis would be identical and fewer computations would be required. The choice of $T = 0.1$ allows more detailed graphs illustrating the smooth growth of the covariance during the time evolution.

Vehicle Model. The continuous-time PVA vehicle model is

$$\dot{x}_v(t) \doteq \begin{bmatrix} 0 & I & 0 \\ 0 & 0 & I \\ 0 & 0 & -\lambda_a I \end{bmatrix} x_v(t) + \begin{bmatrix} 0 \\ 0 \\ I \end{bmatrix} \omega_a(t),$$

where $\omega_a(t)$ is modeled as Gaussian white noise with power spectral density $Q_a = \sigma_a^2$. The corresponding discrete-time description of the PVA vehicle model is approximated as

$$\phi_v = \begin{bmatrix} I & TI & a_3 I \\ 0 & I & a_2 I \\ 0 & 0 & a_1 I \end{bmatrix}, \ \Gamma_v \approx \begin{bmatrix} T^{5/2}/\sqrt{20} I \\ T^{3/2}/\sqrt{3} I \\ \sqrt{T} I \end{bmatrix}, \text{ and } Q_{d_v} = \begin{bmatrix} 0 \\ 0 \\ \sigma_a^2 I \end{bmatrix},$$

with all submatrices being three by three, $a_1 = e^{-\lambda_a T}$,

$$a_2 = \left(1 - e^{-\lambda_a T}\right)/\lambda_a, \quad \text{and} \quad a_3 = \left(\lambda_a T - 1 + e^{-\lambda_a T}\right)/\lambda_a^2.$$

The approximation indicated in Γ_v yields the correct diagonal of the discrete-time noise covariance matrix, but $\Gamma_v Q_{d_v} \Gamma_v^\top$ approximates the off-diagonal terms relative to the exact calculation.

Clock Model. The continuous-time description of the clock model is

$$\dot{x}_v(t) \doteq \begin{bmatrix} 0 & 1 \\ 0 & -\lambda_c \end{bmatrix} x_v(t) + \begin{bmatrix} 0 \\ 1 \end{bmatrix} \omega_c(t),$$

where $\omega_c(t)$ is modeled as Gaussian white noise with power spectral density $Q_c = \sigma_c^2$. The corresponding discrete-time description of the clock model is

$$\phi_c = \begin{bmatrix} 1 & b_2 \\ 0 & b_1 \end{bmatrix}, \ \Gamma_c \approx \begin{bmatrix} T^{3/2}/\sqrt{3} \\ \sqrt{T} \end{bmatrix}, \text{ and } Q_{d_c} = \sigma_c^2,$$

with all matrix elements being scalars and

$$b_1 = e^{-\lambda_c T} \text{ and } b_2 = \left(1 - e^{-\lambda_c T}\right)/\lambda_c.$$

The approximation in Γ_c yields the correct diagonal of the discrete-time noise covariance matrix, but approximates the off-diagonal terms.

Multipath Model. The continuous-time multipath model is

$$\dot{x}_M(t) \doteq -\lambda_M I x_M(t) + \omega_M(t),$$

Copyright ©2018, University of California, Riverside. All Rights reserved.

The corresponding discrete-time multipath model is

$$\phi_M = \gamma_M I, \Gamma_M = \sqrt{T} I, \text{ and } Q_M = \sigma_M^2 I, \text{ with } I \in \mathbb{R}^{\mathrm{m}\times\mathrm{m}}.$$

Model Parameter Values. The parameters describing the Markov model parameters for the acceleration, clock drift, and multipath states are defined in the Tables IV and V. The values in these tables were defined by selecting the correlation time $\tau = \frac{1}{\lambda}$ and steady-state covariance $\bar{P}$ to be reasonable values, then computing:

$$\lambda = \frac{1}{\tau}, \; Q = 2\lambda\bar{P}, \; \gamma = e^{-\lambda T}, \text{ and } Q_d = \bar{P}(1-\gamma^2).$$

The multipath correlation time of 10s was selected for a moving vehicle, for which the reflective surfaces change relatively rapidly.

	λ		$Q = \sigma^2$		$\bar{P} = \frac{Q}{2\lambda}$	
Process	Value	Unit	Value	Unit	Value	Unit
Acceleration	0.1	s^{-1}	1	m^2s^{-5}	5	m^2s^{-4}
Clock drift	1.0	s^{-1}	0.001	m^2s^{-3}	0.0005	m^2s^{-2}
Multipath	0.1	s^{-1}	0.1	m^2s^{-1}	0.5	m^2

TABLE IV: Parameters of the continuous-time Markov process.

	$\gamma = e^{-\lambda T}$	$Q_d = \bar{P}(1-\gamma^2)$	
Process	Value	Value	Unit
Acceleration	0.9905	0.1	m^2s^{-4}
Clock drift	0.9048	$9.06e^{-5}$	m^2s^{-2}
Multipath	0.9905	0.01	m^2

TABLE V: Parameters of the discrete-time Markov process.

C. Risk-Averse Performance-Specified State Estimation

The literature discusses various outlier detection techniques building on fundamental ideas [51]–[56]. RAIM techniques are based on computing a party vector from the measurement residual [57]–[60] assuming that there is enough measurement redundancy to discriminate the outlier source. While many RAIM approaches assume that there is only one outlier, multiple outlier detection has also been well developed [58], [59], [61]–[63]. Extended RAIM (eRAIM) [64] incorporates an Inertial Measurement Unit (IMU) and Kalman filter based estimation into RAIM.

Data redundancy, quantified by the number of degrees-of-freedom (DOFs), is critical to successful outlier accommodation. Both RAIM and eRAIM are based on measurements from a single epoch, limiting data redundancy. Redundancy can be enhanced both by adding additional sensors, multiple GNSS constellations, multiple GNSS frequencies, or by using all sensor data within a sliding temporal window.

The outlier detection problem is fundamentally unobservable, when all measurements have the potential to be affected by outliers [42], [65]. Therefore, outlier detection methods such as those reviewed above are built on outlier hypothesis assumptions, resulting in tests to choose the most likely assumption. When the number of possible hypothesis assumptions is too low, the actual outlier scenario may not be included, but the required level of computations increases with the number and complexity of the assumed fault scenarios.

Recently new methods for outlier accommodation without explicit detection have been presented in the literature. The Least Soft-thresholded Squares (LSS) approach, building on l_1-regularization, that was presented in [66]–[70]. A version of the LSS approach adapted to the sliding time-window problem [71] is presented in [72]. Alternatively, [65] works within an optimization setting to find the largest set of measurements self-consistent with the assumed model. Finally, [42] works within an optimization setting to choose the set of measurements that achieves a performance specification with minimum risk. A main new idea of [42], [65] was to change the focus from detecting outliers to optimal measurement selection. The two papers evaluate optimality by different approaches.

The Risk-Averse Performance-Specified (RAPS) approach [42] specifies the desired level of performance in terms of the posterior information matrix (inverse covariance matrix). Risk is quantified by the norm of the covariance-normalized residual vector. RAPS is able to identify when the performance specification is feasible and to both minimize and quantify the risk associated with the achieved level of performance. The main contribution of [2] is that RAPS was applied to and explained for the GNSS state estimation problem, including both the theoretical derivation and experimental results. The experimental results utilize real-world Doppler and differential pseudorange data, considering the risk associated with both sets of measurements.

In the standard Maximum A Posteriori (MAP) state estimation approach, using all measurements at time k, the negative log-likelihood of the distribution yields the optimization

$$x_k^\star = \underset{x_k}{\operatorname{argmin}} \left(\|x - x_k^-\|_{P_k^-}^2 + \|H_k x_k - z_k\|_R^2 \right), \tag{19}$$

where $\hat{x}_k^-$ represents the optimal a prior estimate at time k. The Kalman filter is the solution to this optimization problem.

The RAPS approach is more general, allowing selection of the state estimate and which measurements to use, subject to the constraint on performance. The RAPS optimization is stated as:

$$\left.\begin{aligned} P1_a : \min_{x,b} & \left[\|x - x_k^-\|_{P_k^-}^2 + \|\Phi(b)(Hx - z_k)\|_R^2 \right] \\ \text{subject to: } & H^\top R^{-1}\Phi(b)H + J_k^- \geq J_l \\ & b_i \in \{0,1\} \text{ for } i = 1,\ldots,m, \end{aligned}\right\} \tag{20}$$

where J_k^- is the prior information matrix, J_l is a lower bound on the posterior information matrix $H^\top R^{-1}\Phi(b)H + J_k^-$, b is the measurement selection vector, and $\Phi(b) = diag(b)$. The cost function

$$C(x,b) = \|x - x_k^-\|_{P_k^-}^2 + \|\Phi(b)(Hx - z_k)\|_R^2$$

quantifies the risk. Variants of this problem and alternate solution methods are discussed in [42]–[44].

Copyright ©2018, University of California, Riverside. All Rights reserved.